Large Magnetoresistance and High Spin-Transfer Torque Efficiency of $Co_2Mn_xFe_{1-x}Ge$ ($0 \leq x \leq 1$) Heusler Alloy Thin Films Obtained by High-Throughput Compositional Optimization Using Combinatorially Sputtered Composition-Gradient Film

Vineet Barwal*, Hirofumi Suto*, Ryo Toyama, Kodchakorn Simalaotao, Taisuke Sasaki, Yoshio Miura and Yuya Sakuraba

Research Center for Magnetic and Spintronic Materials,

National Institute for Materials Science (NIMS), Tsukuba, 305-0047, Japan

*BARWAL.Vineet@nims.go.jp

*SUTO.Hirofumi@nims.go.jp

ABSTRACT

Half-metallic ferromagnetic Heusler alloys having high spin polarization are the promising candidates to realize large magnetoresistance (MR) ratio and high spin-transfer torque (STT) efficiency in next-generation spintronic devices. Since Heusler alloy properties are sensitive to composition, optimizing the composition is crucial for enhancing device performance. Here, we report the fabrication of high-performance current-perpendicular-to-plane giant magnetoresistance (CPP-GMR) devices using $Co_2Mn_xFe_{1-x}Ge$ ($0 \leq x \leq 1$) Heusler alloy, employing high-throughput and detailed composition optimization method. The method combined composition-gradient films and local measurements to enable the composition variation from Co_2FeGe to Co_2MnGe to be efficiently studied on a single library sample with a small composition interval. The CPP-GMR devices fabricated from stacks annealed at 250°C showed a clear composition dependence of MR with the maximum of MR ratio ~ 38% in the Mn-rich region of x = 0.85. By increasing the annealing temperature to 350°C, the MR ratio increased to ~ 45% along with high STT efficiency ~ 0.6 in the broad composition range of $0.2 \leq x \leq 0.7$. The optimal composition for the highest MR changed with annealing temperature because of the stability of the GMR stack being higher in the lower x range. The record high MR for the all-metal CPP-GMR devices, at low annealing temperature of 250°C was achieved by the detailed composition optimization. These results present the high potential of $Co_2Mn_xFe_{1-x}Ge$ and provide a comprehensive guidance on the composition optimization for achieving large MR ratio and high STT efficiency in the CPP-GMR devices.

I. INTRODUCTION

Half-metallic ferromagnetic (HMF) Heusler alloys are an important class of materials for spintronic applications due to 100% spin polarization (P) as predicted by their electronic band structure [1,2]. Co-based HMF Heusler alloy are the promising Heusler candidates owing to high $P \sim 100\%$ and high Curie temperature (T_c) far above room temperature. For example, employing HMF Heusler alloys such as Co_2MnSi (CMS)[3], $Co_2Fe_{0.4}Mn_{0.6}Si$ (CFMS)[4–8], $Co_2FeAl_{0.5}Si_{0.5}$ (CFAS)[9], $Co_2FeGa_{0.5}Ge_{0.5}$ (CFGG)[10,11] thin films as ferromagnetic (FM) electrodes in current-perpendicular-to-plane giant magnetoresistance (CPP-GMR) demonstrated large magnetoresistance (MR) ratio ~ 40% with typical resistance area (RA) ~0.05 $\Omega\mu m^2$. These all metallic CPP-GMR device with large MR and low RA show potential for read sensors for next-generation hard disk drives (HDDs) with data recording density beyond 4 Tbit/inch^2.[7,12–17] The increase in areal density of HDDs require scaling down the size of read-head sensors with sufficient signal-to-noise (SNR) ratio and a high bit resolution. At reduced sensor dimension, the lower impedance of CPP-GMR structure provides an advantage over tunnel magnetoresistance (TMR) based FM/insulator/FM magnetic tunnel junction (MTJ) structure for read-head sensors. The large MR ratio and low impedance in CPP-GMR devices results in obtaining high SNR ratio which is significant for high density recording in HDDs. Highly spin polarized Heusler alloys can also achieve high spin-transfer-torque (STT) efficiency (η) in addition to high MR.[2,18,19] Both, MR and η depends on the spin polarization of conduction electrons in FM layers of CPP-GMR and MTJs. The required current density for STT-induced magnetization switching in STT magnetoresistive random access memory (MRAM) and STT-induced persistent oscillations of magnetization in spin-torque oscillators (STOs) is inversely proportional to the η parameter. Higher STT efficiency results in lower operational current for STT MRAMs making them more energy efficient and enhancing the endurance[20]. Also, high η in STOs results in large-amplitude magnetization oscillation of large magnetic volume which is necessary to attain higher magnitude of

generated microwave field [21–24]. Thus, high STT efficiency is significant for the efficient operation of STT-MRAMs and STOs.

Studies have demonstrated that the structural and magnetic properties such as P, T_c, and Gilbert damping of Heusler alloys are very sensitive to and can be controlled by composition[25–27]. Compositional tuning of Heusler thin films as FM electrodes in CPP-GMR devices is carried out to enhance the device performance[5,28,29]. This is generally done for selected compositions of Heusler, through stack deposition and device fabrication for each composition, which is time- and resource-consuming. The combinatorial sputtering can break through the limitation by enabling efficient and systematic investigation of a wide range of material compositions on a single library sample.[30,31] We recently studied the MR and STT efficiency in CPP-GMR devices containing composition-gradient Co_xFe_{1-x} ($0 \leq x \leq 1$) system at fine x interval.[32] The approach significantly enhanced the throughput of the material synthesis and characterization but has never been applied for the CPP-GMR with the HMF Heusler electrodes.

In addition to the composition tuning, the HMF Heusler alloys for spintronic applications often require higher degree of atomic order because the half-metallic energy gap is collapsed by the atomic disorder and the formation of detrimental antisites.[17,33,34] For several potential applications such as the read head of HDDs, high atomic order is required to be obtained at lower process temperature around 300°C. Among half-metallic Co-based Heusler alloys, Co_2MnGe (CMG) and Co_2FeGe (CFG) are considered the most suitable for achieving high atomic order through low-temperature annealing. This is because they are intermetallic compounds with high order-disorder transition temperatures, indicating high thermal stability of the $L2_1$-ordered structure. Such alloys are expected to show very high driving force for the chemical ordering from the disordered state in thin films. Therefore, $Co_2Mn_xFe_{1-x}Ge$ (CMFG), the mixture of CMG and CFG should have a high chemical ordering behavior at low-temperature annealing[35]. There are several studies on CMFG Heusler based CPP-

GMR devices using $Co_2Mn_{0.6}Fe_{0.4}Ge$ (x = 0.6) [36–39]. Other than this composition, Page *et al.* investigated the properties of polycrystalline $Co_2Mn_{1-x}Fe_xGe$ (x = 0, 0.1, 0.2, 0.4) Heusler alloy FM layer within the CPP-GMR spin valves and found high MR ratio of ~15% (change in resistance area product $\{\Delta RA\}$ ~ 6 mΩ μm^2) independent of Fe content[40]. Nakatani *et al.* reported that the MR ratio did not change significantly by varying Mn and Fe concentrations within the observed range for the polycrystalline CMFG. They found that the Co:Mn(Fe) ratio has a wide window for obtaining large MR ratio, while the Co:Ge ratio needs to be tuned to 2:1 in order to maximize the CPP-GMR output[35]. However, no studies for the epitaxial CMFG films within the CPP-GMR stacks have been done varying the composition, especially Mn:Fe ratio, in fine increments. In the previous studies involving tuning of Fe/Mn ratios (x) in $Co_2Fe_xMn_{1-x}Si$/Ag/ $Co_2Fe_xMn_{1-x}Si$ CPP-GMR devices with various x, it was shown that the addition of Fe in CMS improved the interfacial exchange stiffness of Co at the Ag spacer, resulting in an enhancement of interfacial spin scattering asymmetry parameter, thereby increasing the MR ratio[5]. This indicates that the tuning of Mn/Fe ratio in CMFG is crucial to obtain high MR and STT in CPP-GMR devices.

Here, we report the large MR ratio and high STT efficiency in CPP-GMR devices containing epitaxial $Co_2Mn_xFe_{1-x}Ge$ ($0 \leq x \leq 1$) Heusler alloy thin films achieved through the high throughput and detailed composition optimization method. Combinatorial sputtering method was employed to achieve a composition variation from CFG to CMG on a single library sample. The samples were analyzed locally at the various composition points by X ray diffraction (XRD), MR measurement, and scanning transmission electron microscopy (STEM), thereby enhancing the throughput and resolution in characterization. We observed a clear composition dependence of MR for the CPP-GMR stacks annealed at 250°C, with the maximum MR ratio ~ 38% in the Mn-rich region of x = 0.85. By increasing the annealing temperature to 350°C, the MR ratio was increased to 45% along with high STT efficiency ~ 0.6 over a broad composition range ($0.2 \leq x \leq 0.7$). At 350°C annealing, the optimum

composition shifted to lower *x* range as the stability of the GMR stack was higher in this *x* range. The results reveal efficient composition tuning and provides comprehensive guidance for the selection of CMFG composition to obtain large MR ratio and high STT efficiency in the CPP-GMR devices.

II. EXPERIMENTAL AND COMPUTATIONAL DETAILS

A. Sample growth and device fabrication

Epitaxial thin film stacks including CMFG composition-gradient layers were deposited on 2×2 cm^2 MgO (001) substrate using combinatorial sputtering system (CMS-A6250X2, Comet, Inc.). The base pressure was lower than 6×10^{-6} Pa. Prior to deposition, the MgO substrates were cleaned by ultrasonication with acetone, ethanol, and de-ionized water for 5 minutes each, followed by *in-situ* flash annealing at 600°C for 30 minutes in the deposition chamber. Figure 1(a) and 1(b) illustrate two different stack configurations named Type-I, and Type-II, respectively. The Type-I stack were comprised of CPP-GMR stack with both magnetic layers being $Co_2Mn_xFe_{1-x}Ge$, which was used to evaluate the MR output of the devices. The Type-II stack was comprised of CPP-GMR stack with magnetic layers being $Co_2Mn_xFe_{1-x}Ge$ and $Ni_{80}Fe_{20}$, which was used for the STT measurement. The Type-II stack was designed to have a thicker CMFG bottom electrode (~15 nm) as compared to the top NiFe (~7 nm) to make the CMFG layer resistant to the STT from the NiFe layer. The bottom CMFG acting as a spin injection layer (SIL) induces STT and reverses the magnetization of the top NiFe layer acting as a free layer (FL). Three Type-I sample stacks with different thermal treatments were prepared: as-deposited sample and samples subjected to *in-situ* post-annealing at 250°C and 350°C for 30 min, respectively. For the Type-II stack, sample with 350°C post annealing was prepared. The red arrows in the figure 1(a) and 1(b) indicate the layer after which *in-situ* post annealing was done. The top 8 nm Ru cap layer was deposited after cooling down the sample to room temperature. Note that there was a difference between the set temperature at the controller and the actual temperature at the substrate. For example, the set temperature of 200°C (300°C) at the controller

attains maximum actual temperature ~ 250°C (350°C) at the substrate because of the overshooting in heating process and reaches to ~ 220°C (320°C) in about 30 minutes (annealing time in the present experiment). Here, we used the maximum actual temperature at the substrate (250°C or 350°C) for simplicity.

The CFG(CMG) film was deposited by co-sputtering of $Co_{67}Fe_{33}$($Co_{60}Mn_{40}$) and Ge targets using DC and RF power sources. The actual compositions for the Co_2MnGe and Co_2FeGe nominal compositions films were calibrated separately using X-ray fluorescence (XRF) spectroscopy, yielding values of $Co_{54.49}Mn_{23.65}Ge_{21.86}$ and $Co_{47.11}Fe_{30.88}Ge_{22.01}$, respectively. Figure 1(c) illustrates the combinatorial sputtering process. The CMFG composition-gradient film was obtained by the alternating deposition of CFG and CMG wedge-shaped layers using a linear moving mask and substrate rotation in the manner described below. We have used the similar combinatorial sputtering process in our previous studies to obtain well-controlled composition gradient film[25,32,41,42].

1. CFG deposition: wedge-shaped CFG layer was deposited using a linear moving mask, defined to move along the *X* direction from -6 to +6 mm with respect to the center of the substrate. This corresponds to the composition-gradient width of 12 mm with a thickness gradient of 0 to 0.5 nm from -6 mm to +6 mm and the uniform CFG region from -9.5 to -6 mm. The speed of the mask was determined by the deposition rate of CFG (0.16 Å/s). ensuring a maximum thickness for one-unit layer of 0.5 nm. This thickness was chosen to be close to the lattice parameter of the Heusler alloys.
2. Substrate rotation: The substrate was rotated by 180°.
3. CMG deposition: Wedge-shaped CMG layer was then deposited using the mask moving along the *X* direction from -6 to +6 mm with respect to the center of the substrate, at a speed determined by the CMG deposition rate (0.30 Å/s), which corresponds to the composition-gradient width of 12 mm with a thickness gradient of 0 to 0.5 nm and the uniform CMG

region from -9.5 to -6 mm.

4. Cyclic process: Steps 1 to 3 producing flat 0.5-nm-thick one-unit layer of CMFG was repeated 2*n* times to obtain the desired thickness of *n* nm.

The *X* axis in Fig 1(a), and 1(b), corresponds to the composition-gradient direction and the dotted lines on the stacks indicate the separation between the composition-gradient region at the center and uniform composition region for the CFG and CMG on the left and right side of the sample. The software was equipped with a recipe option so that the deposition can be completed in an automated mode. Figure 1(d) shows the variation of estimated composition for the CMFG film along the *X* axis, calculated using the compositions of CFG and CMG determined by XRF. Upper abscissa scale shows the variation of nominal Mn content (*x*) from 0 (CFG side) to 1 (CMG side). The actual composition can be deduced from the nominal *x* content by using the formula:

$$CMFG = x \times (Co_{CMG} + Mn_{CMG} + Ge_{CMG}) + (1 - x) \times (Co_{CFG} + Fe_{CFG} + Ge_{CFG}), \quad (1)$$

where $N_{\mathrm{CMG/CFG}}$ represents the composition of $N(\mathrm{Co/Mn/Ge})$ atom in CMG/CFG, determined from XRF measurement.

For the CPP-GMR device fabrication, the Type-I and Type-II sample were patterned into circular and elliptical pillars with designed dimensions (80 × 80 nm^2, 140 × 70 nm^2, 100 × 100 nm^2, and 200 × 100 nm^2) using a combination of electron-beam lithography, photolithography and Ar-ion milling techniques. After patterning, the pillars were passivated by a SiO_2 layer, and an Au top electrode was deposited. The pillars with different size were distributed across 20 rows and 64 columns with a fixed pillar size in a row and 5 rows for each device size. The composition-gradient region of 12 mm was approximately divided into 48 columns by fabricating pillars at an interval of 250 μm. A total of 20 devices at one composition were fabricated.

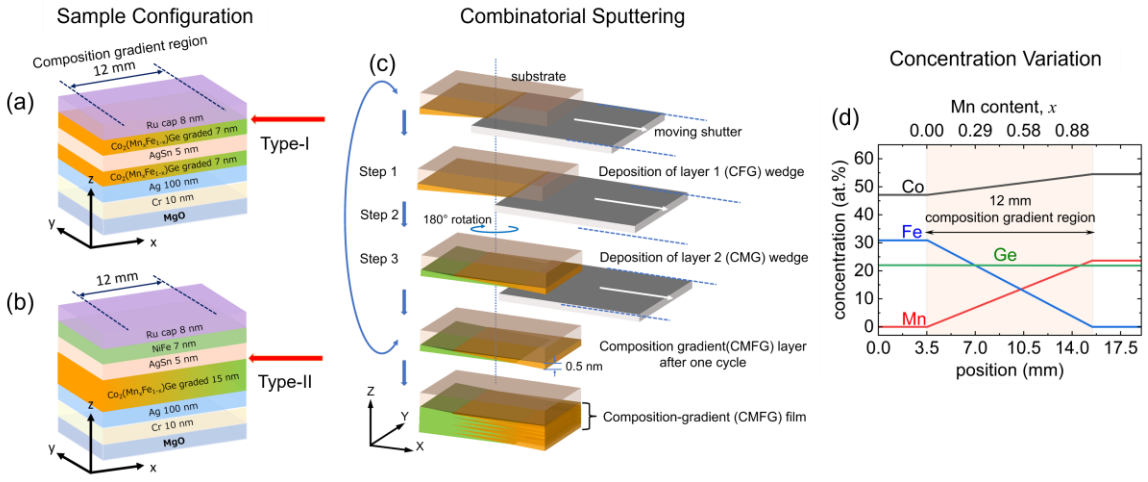

FIG. 1. Sample configuration for the (a) Type-I and (b) Type-II sample structures with red arrows indicating layer after which *in-situ* post annealing was done. (c) Schematic showing the combinatorial sputtering deposition process. (d) Variation of atomic concentration in $Co_2Mn_xFe_{1-x}Ge$ composition-gradient film along the *X* axis. The shaded region highlights the 12 mm composition-gradient width across the 19 mm deposition length scale.

B. Characterization

Structural characterization was done using XRD equipped with a Cu K_α radiation source ($\lambda = 1.5418$ Å) for the Type-I sample stacks prior to the device fabrication. The X-rays were collimated using a 0.5 mm incident slit and irradiated at various positions in steps of 1 mm along the *X* axis to span the gradient as well as the uniform composition regions. The XRD scans were recorded using a two-dimensional X-ray detector.

The resistance versus magnetic field (*R*-*H*) measurements were carried out for the Type-I and Type-II samples on the CPP-GMR devices with all four pillar sizes using an auto prober system via four-probe method applying in-plane magnetic field in the range of ± 30 mT. For the MR analysis, the data points were filtered based on the observed R_P (resistance in the parallel configuration), ensuring they fell within ± 30% of the device resistance calculated using the resistivity values for each layer and

the designed pillar size. The parasitic resistance ($R_{parasitic}$) was then determined by plotting $\Delta R = |R_P - R_{AP}|$ (where R_{AP} is the resistance in the anti-parallel configuration) as a function of R_P and then linearly fitting the data points to extract $R_{parasitic}$, which corresponds to the R_P intercept at $\Delta R=0$. The $R_{parasitic}$ was typically around 0.5 Ω. Intrinsic MR ratio was calculated using the formula $(|R_P - R_{AP}|)/(R_P - R_{parasitic}) \times 100\%$. For each composition, the average MR ratio was calculated and devices showing a deviation of more than ± 20% from the average were considered defective and their data excluded. Observed MR ratio was calculated using the formula $(|R_P - R_{AP}|)/R_P \times 100\%$. The ΔRA was calculated using the designed device area. STT induced magnetization reversal measurements were carried out for the Type-II sample with circular pillars having designed diameter of 80 nm. The circular pillar's cross-sectional area was estimated to be approximately 10.58×10^{-3} μm^2 using scanning electron microscopy. We used the recently proposed method of STT induced magnetization reversal against the magnetic field to evaluate the STT efficiency[43]. The method provides straightforward approach to analyze STT efficiency in the fabricated CPP-GMR devices. The STT efficiency can also be evaluated through alternative techniques that involve STT-induced magnetization dynamics. These methods include inducing magnetization switching of a magnetic layer with magnetic anisotropy or conducting spin torque ferromagnetic resonance (FMR) measurements. The former method is affected by stochastic switching, influenced by thermal fluctuations in magnetization, while the latter necessitates high-frequency measurements at FMR frequencies (typically in the GHz range) and requires precise calibration of bias current, as signals at these frequencies are prone to attenuation. In contrast, the magnetization switching in the present method is achieved solely by the balance between STT and damping, allowing us to neglect thermal effects, which simplifies the analysis.

High-angle annular dark-field scanning transmission electron microscope (HAADF-STEM) observations and energy-dispersive X-ray spectroscopy (EDS) were performed for the Type-I sample stacks using a FEI Titan G2 80-200 TEM with a probe aberration corrector operating at 200 kV. Thin

foil specimens for STEM observations were prepared by the focused ion beam lift-out technique using a FEI Helios G4 UX.

C. Computational Methods

A model of the $L2_1$ Heusler structure was employed, consisting of four atoms arranged on interpenetrating face-centered cubic (fcc) sublattices. Specifically, the basis included two Co atoms at (0, 0, 0) and (0.5, 0.5, 0.5), one Ge atom at (0.75, 0.75, 0.75), and disordered Mn and Fe atoms at (0.25, 0.25, 0.25), with a composition ratio of Mn_xFe_{1-x} ($0 \leq x \leq 1$). The lattice parameter (a) for the $L2_1$ ordered $Co_2Mn_xFe_{1-x}Ge$, was determined by applying Vegard's law, interpolating between the identical lattice parameters of the terminal alloys, Co_2FeGe [44] and Co_2MnGe[45]. The determined lattice parameter, a = 5.743 Å was used for all the calculations. Based on density functional theory (DFT), the generalized gradient approximation (GGA) proposed by Perdew, Burke, and Ernzerhof (PBE) [46] was adopted for the exchange and correlation energy. The calculations were performed using the Vienna ab initio simulation package (VASP)[47,48] code with the projector-augmented wave (PAW) [49,50]method. The kinetic energy cutoff for the plane-wave basis set was set as 400 eV. Atomic disorder is described by the virtual crystal approximation (VCA)[51]. Numerical Brillouin zone (BZ) integrations are performed by using Monkhorst-Pack[52] special k-point meshes of 10 × 10 × 10 for self-consistent field calculations and 20 × 20 × 20 for density of states (DOS) calculations.

III. RESULTS AND DISCUSSION

A. Effect of Mn/Fe ratio in CMFG on the electronic states of CMFG

In order to investigate the effect of Mn:Fe composition on the spin polarization of $Co_2Mn_xFe_{1-x}Ge$, we calculated the spin resolved DOS. Figure 2(a) and 2(b) shows the calculated energy dependence of the *spd*- and *sp*-orbital DOSs for $L2_1$-ordered $Co_2Mn_xFe_{1-x}Ge$ ($0 \leq x \leq 1$) at an x interval of 0.1, respectively. The calculations clearly demonstrate a shift in E_F position with respect to composition, while the overall DOS shape is preserved. The spin polarization was calculated using the standard definition $P[\%] = 100 \times (D_\uparrow - D_\downarrow)/(D_\uparrow + D_\downarrow)$, where $D_\uparrow$ and $D_\downarrow$ are the majority- and minority-spin DOSs at the Fermi level (E_F). From the previous studies, it is known that the *sp* electrons having small effective mass contributes majorly to the electrical conduction process and thus *sp* spin polarization (P_{sp}) is a good representative parameter for the spin-dependent transport in the CPP-GMR devices. Figure 2(c) shows the calculated energy dependence of P_{sp} of $L2_1$-ordered CMFG ($0 \leq x \leq 1$), and Fig. 2(d) shows x dependence of the higher and lower energy edge of the gap estimated at $P_{sp} = 95$ %. The E_F was observed to be inside the gap for $0.3 \leq x \leq 1$, indicating the almost half-metallic character, as confirmed in the P_{sp} at E_F (Fig.2(c) inset). Because high P and E_F position close to the gap center are considered beneficial for obtaining large MR ratio and high STT efficiency, these results indicate that there is an optimal range of x.

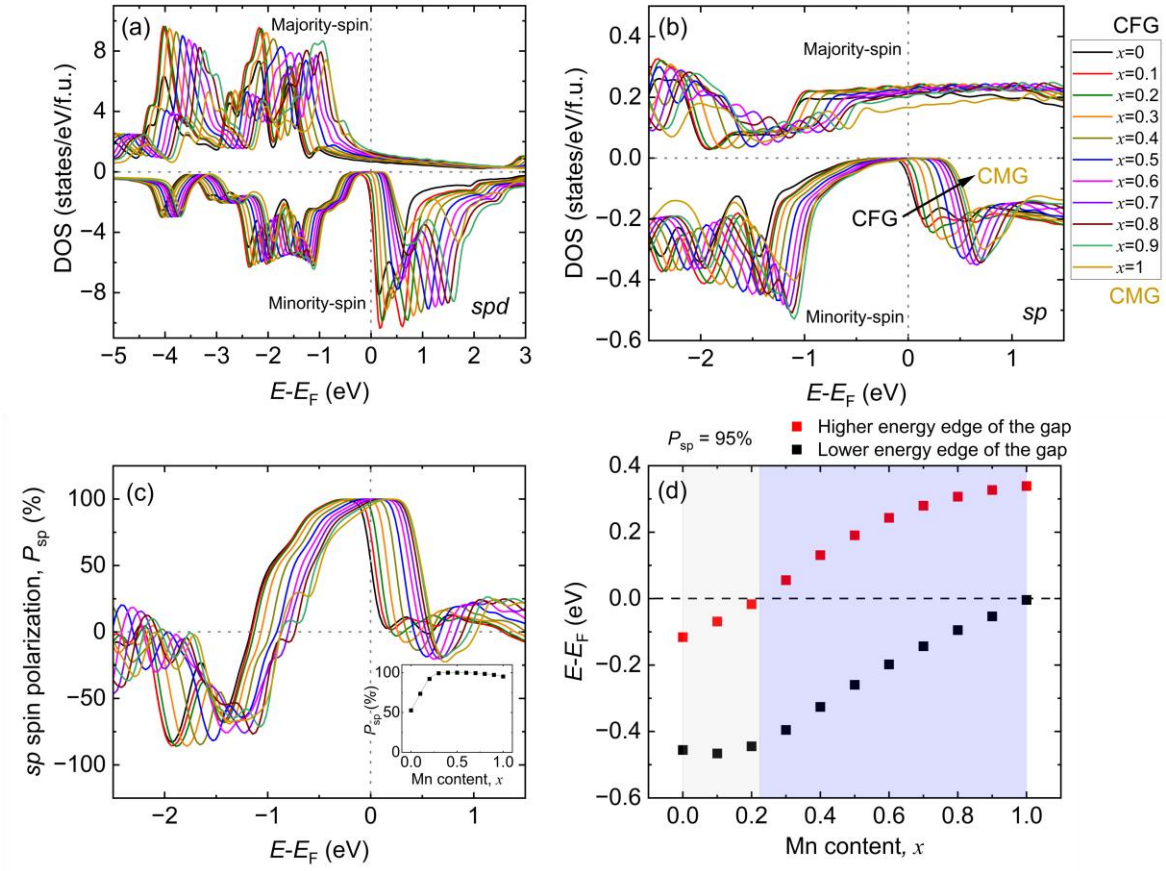

FIG. 2 First-principles calculations of the (a) *spd*-total DOSs, (b) *sp*-orbital DOSs and (c) *sp* spin polarization (P_{sp}) for the $L2_1$-ordered $Co_2Mn_xFe_{1-x}Ge$ ($0 \leq x \leq 1$) at an x interval of 0.1. Inset in (c) shows the change in P_{sp} with Mn content, x. (d) Higher and lower energy edge of the gap estimated at P_{sp} = 95 % for different Mn content ($0 \leq x \leq 1$) at an x interval of 0.1. The legends are common for (a), (b) and (c).

244

B. XRD analysis

Figure 3a illustrates the orientation relationship for the CMFG film epitaxially grown on MgO (001) substrates with MgO (001) ‖ Cr(001) ‖ Ag (001) ‖ CMFG (001) and MgO[100] ‖ Cr[110] ‖ Ag [100] ‖ CMFG [110]. Figure 3b, 3c and 3d shows the out of plane θ-2θ XRD scans at $\chi = 0°$ and 54.7° of the Type-I sample stack at the selected Mn compositions (x =1, 0.92, 0.75, 0.58, 0.42, 0.25, 0.08, and 0) for the as-deposited, 250°C and 350°C post-annealed (PA) samples, respectively. The lattice parameter evaluated from the 004 diffraction peak shows negligible change with composition, being 0.575 ± 0.001 nm from the CFG to the CMG side. The lattice mismatch between CMFG and Ag is estimated to be < 0.5% from the lattice parameter (a = 0.574 nm) of the-bulk CMFG and $\sqrt{2}a$ = 0.577 nm for Ag. This value matches well with the reported value [40]. The 111 superlattice peaks were detected by tilting the sample at χ = 54.7° with respect to the film-surface normal direction. The observation of the low intensity 002 superlattice diffraction peak in the as-deposited sample shows large $A2$-type disorder with the presence of partial $B2$ ordering (atomic order between Co and (Fe, Mn, Ge) sites. The enhancement in the intensity of the 002 diffraction peak along with the appearance of low intensity 111 diffraction in the 250°C PA sample shows the enhanced $B2$ ordering and presence of $L2_1$ ordered phase (atomic order between (Fe, Mn) and Ge sites) in the sample. Further enhancement of the 002 and 111 superlattice diffraction peak intensity for the 350°C PA sample shows the enhancement of the $B2$ and $L2_1$ ordering with annealing temperature, respectively.

For the 350°C PA sample, low-intensity peak at 2θ = 75.5° was observed at the $\chi = 0°$ scan for the Mn-rich compositions (x = 1 and 0.92), marked by the symbol ♣. This peak can be attributed to secondary phase at higher annealing temperature and possibly due to diffraction from either one or a combination of hcp $Co_{1.75}Ge$ 004, or fcc Co 220 or hcp Co 110 planes[53].

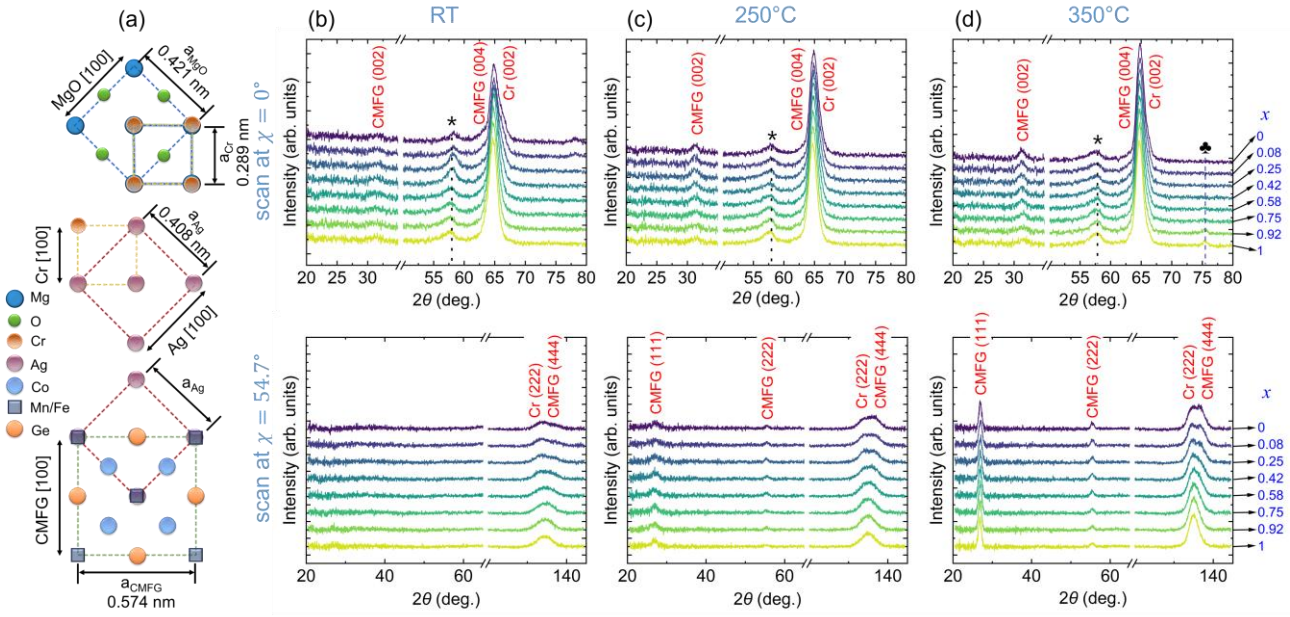

FIG. 3. (a) Schematic showing fcc MgO 001, bcc Cr 001, fcc Ag 001, $Co_2Mn_xFe_{1-x}Ge$ (CMFG) Heusler 001 plane with epitaxial relationship between MgO and Cr; Cr and Ag; and Ag and CMFG. θ-2θ XRD scans for the Type-I structures along the 002 and 111 plane at χ = 0°and χ = 54.7° respectively, for the (b) as-deposited sample, (c) 250°C and (d) 350°C post-annealed sample. The * symbol marks the peak position for the Ru 102 plane and ♣ marks the peak position for the hcp $Co_{1.75}Ge$ 004, or fcc Co 220, or hcp Co 110 planes.

267

C. Magnetotransport properties

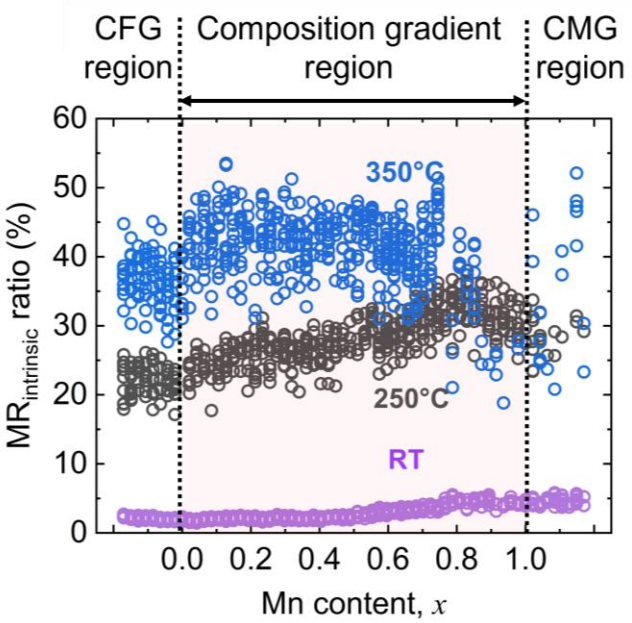

FIG. 4. Change in intrinsic magnetoresistance (MR) ratio with Mn content for the Type-I CPP-GMR sample stack with different annealing temperatures.

We studied the MR output for the CPP-GMR devices fabricated from the Type-I samples. Figure 4 shows the intrinsic MR ratio variation with Mn content for the as-deposited, 250°C PA and 350°C PA samples. The change in observed MR ratio and ΔRA with respect to Mn content is shown in figure S1(a) and S1(b) in the supplementary material, respectively. In-plane *R-H* curves for the as-deposited, 250 °C and 350 °C PA Type-I samples at three different compositions viz. Co_2FeGe, $Co_2Mn_{0.5}Fe_{0.5}Ge$ and $Co_2Mn_{0.9}Ge_{0.1}$.are shown in the supplementary figure S2. In the as-deposited sample, the MR ratio exhibited gradual change with Mn content. The CFG side showed lower MR ratio ~ 2.5% and the CMG side showed slightly higher MR ratio ~ 5%. In the 250°C PA sample, the MR was greatly enhanced and exhibited the following clear composition dependence. The maximum MR ratio was ~ 25% at $x = 0$, increased gradually with increasing x, and showed a maximum MR ratio of ~38% at

around x= 0.85. Then it decreased to the CMG side. In the 350°C PA sample, MR was further enhanced with maximum MR ratio of ~ 45% in the broad x range. The trend of MR ratio versus x changed from the case of 250°C PA sample. First, it increased in the x range of 0-0.2, stayed almost constant in broad x range of 0.2-0.7, and then abruptly decreased near the CMG side. In addition, the distribution in MR increases significantly with increased annealing temperature. The MR analysis was also performed for the 350°C PA Type-II sample, see figure S3 and S4 in the supplementary material. A drop in MR was observed around the pure CMG side (x = 1), as observed in the 350°C PA Type-I sample.

An overall improvement in MR ratio with increasing annealing temperature can be attributed to the enhanced atomic order with increasing annealing temperature, as discussed in the following. Atomic ordering in Heusler is very crucial to obtain good magnetic properties. In-general, for Co_2YZ (Y = Cr, Mn and Z = Si, Ge, Al) HMF Heusler compounds, the perfectly ordered structure has the highest P. While the $B2$ type disorder (swapping between Y and Z sites) does not reduces P significantly, the $A2$ type disorder (swapping between Co and Y/Z sites) reduce P considerably[3334]. The MR ratio in CPP-GMR devices being proportional to P of FM electrodes, is enhanced with increasing annealing temperature. The as deposited sample mainly showed *A2* disordered phase and exhibited low MR ratio. On increasing PA temperature to 250°C we observed significant enhancement in MR ratio due to enhanced $B2$ ordering in the sample. The MR ratio increased further as the $L2_1$ ordering sets in for the 350°C PA sample. The maximum MR ratio for the 250°C PA Type-I sample reached to a high value of 38% around x = 0.85. In contrast, the 350°C PA Type-I sample showed the drop in MR ratio at x = 0.85, which was optimum at 250°C, deteriorated at 350°C. The drop in MR ratio can partially be attributed to the existence of secondary phase in the CMG side, as observed in the XRD. Interdiffusion of CMFG with Ag buffer and spacer is also expected to affect the MR property, which we will discuss later from the STEM observation. As a result, the optimal composition range shifted

to the lower x for the 350°C PA Type-I sample, and maximum ΔRA values in the range ~ 4 – 8 mΩ μm² was observed (see figure S1(b) in the supplemental material). The high MR ~ 38 % for x = 0.85 and MR ~ 45 % for x range of $0.2 \leq x \leq 0.7$ in CMFG was achieved at relatively low annealing temperature of 250°C and 350°C, respectively. These MR values are the highest among all-metal CPP-GMR devices at lower annealing temperatures (Ref. table S1 in the supplementary material {see also references [54–57] therein}).

D. Cross sectional TEM observation

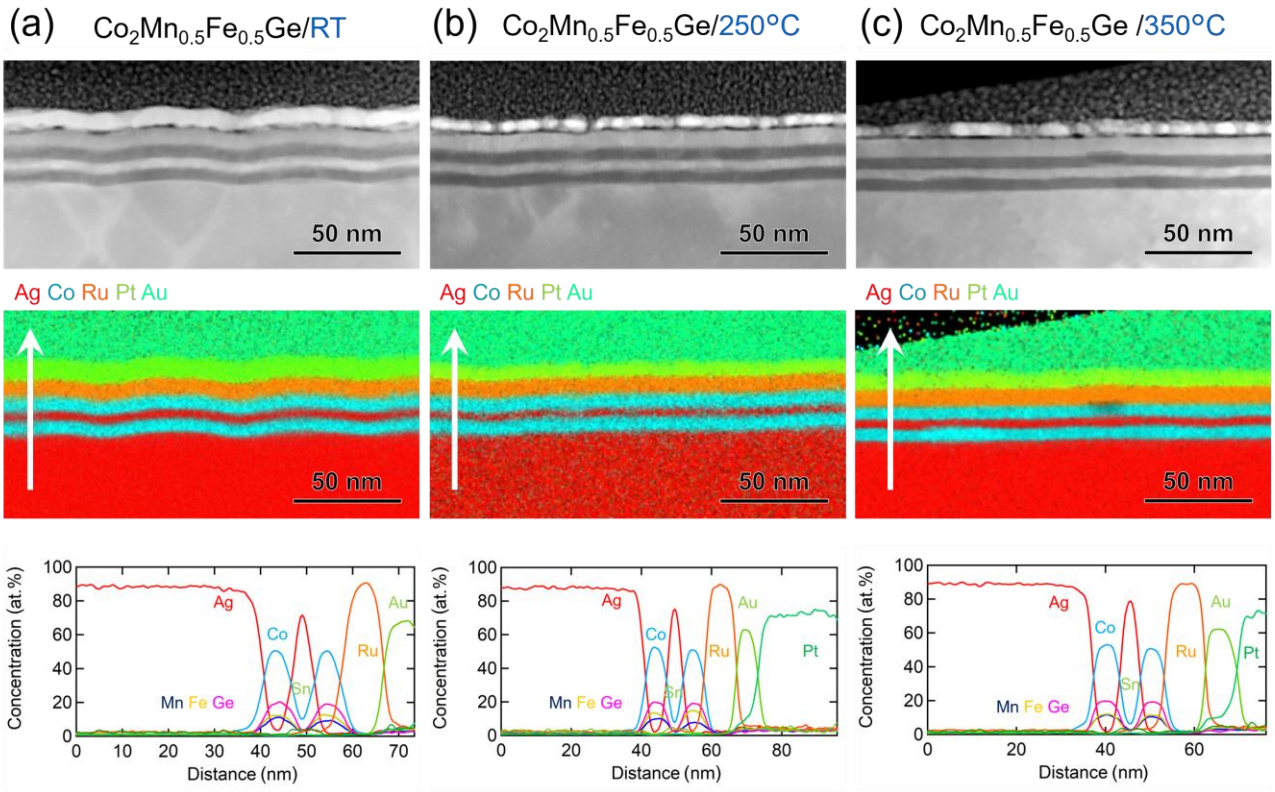

FIG. 5. Cross sectional HAADF-STEM images along with EDS elemental maps of Ag, Co, Ru, Pt and Au and the corresponding EDS line profile along the direction indicated by white arrow for the (a) as-deposited, (b) 250°C and (c) 350°C PA Type-I sample at x = 0.5 in CMFG.

We performed cross-sectional TEM analysis to elucidate the effect of annealing temperature and

composition on the interface between the spacer and the CMFG layers. Figures 5(a), (b) and (c) show the cross-sectional HAADF-STEM images for the as-deposited, 250°C and 350°C PA Type-I samples at the composition of x = 0.5 along with EDS elemental maps of Ag, Co, Ru, Pt, and Au and the corresponding EDS line compositional profile analyzed along the direction indicated by the white arrow. We see clear and well separated interfaces of the CMFG layers with Ag buffer and AgSn spacer layer for the as-deposited, 250°C and 350°C PA Type-I samples. The surface roughness/irregularity in the Ag buffer was observed to propagate to the successive CMFG, AgSn and Ru layers in the as-deposited sample. Interestingly, the film flatness improves with increasing annealing temperature for the 250°C and 350°C PA samples. The composition of the CMFG layer from the EDS line profiles matches well with the composition values obtained from the XRF results.

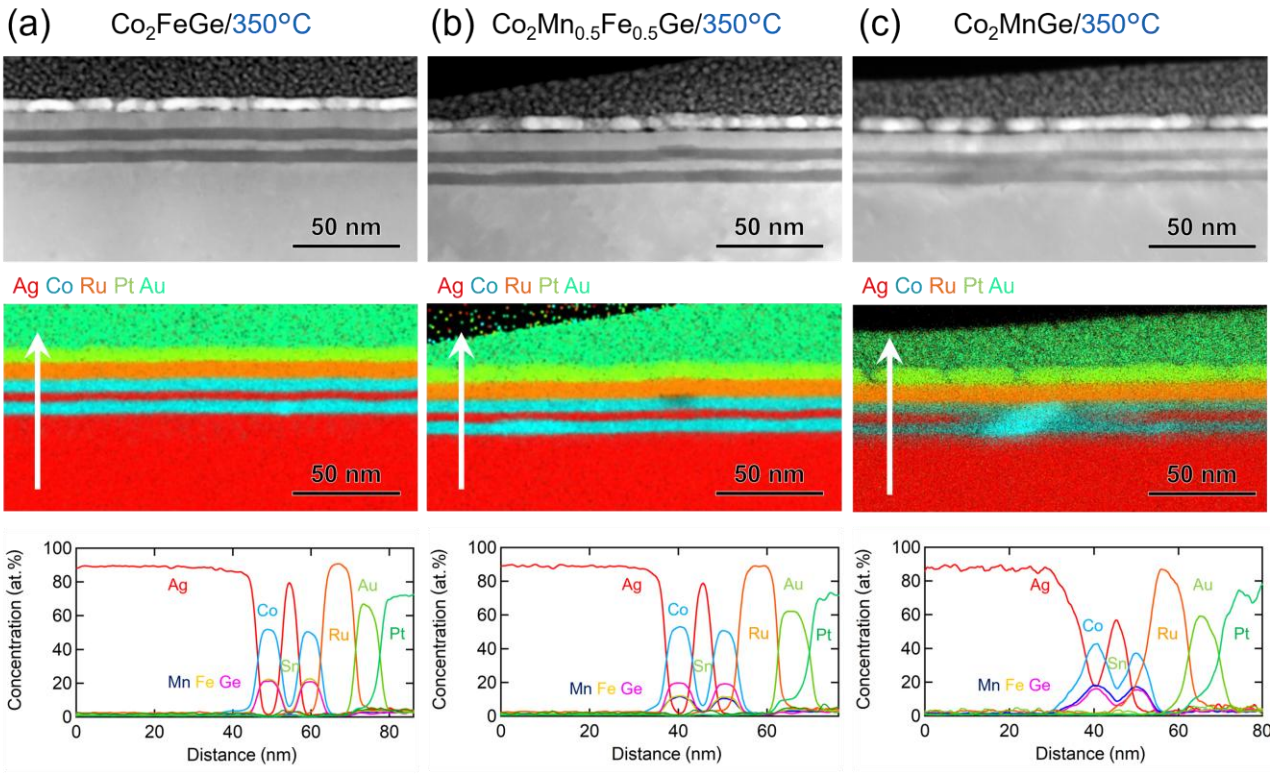

FIG. 6. Cross sectional HAADF-STEM images along with EDS elemental maps of Ag, Co, Ru, Pt

and Au and the corresponding EDS line profile along the direction indicated by white arrow for the (a) $x = 0$ [CFG], (b) $x = 0.5$ [$Co_2Mn_{0.5}Fe_{0.5}Ge$] and (c) $x = 1$ [CMG] composition for the 350°C PA Type-I sample.

Figure 6 shows the cross-sectional HAADF-STEM images of the 350°C PA Type-I sample at three different compositions, viz. $x = 0$, 0.5 and 1. The EDS elemental maps of Ag, Co, Ru, Pt, and Au and the corresponding EDS line compositional profile are analyzed along the direction indicated by white arrow. The interface between the spacer and CMFG layers is sharp without interdiffusion of the constituent elements for $x = 0$ and $x = 0.5$. In contrast, significant interdiffusion of the constituent elements was observed in the spacer and CMFG layers in $x = 1$, resulting in a gradual change in the composition profile. In addition, the spacer became discontinuous as the Co-rich phase was formed through the spacer. The drop in MR ratio for the $x = 1$ CMFG composition can be attributed to the change in the chemical composition of the Heusler alloy electrodes and the formation of the discontinuous spacer region by interdiffusion. Our result is consistent with the report that Co_2FeZ type Heusler alloy shows high thermal tolerance for a Ag spacer in comparison to the Co_2MnZ type Heusler[10]. The fact that Fe has lower solubility in Ag than Mn increases the robustness of the interface between the Fe rich composition in CMFG and Ag in the multilayered structure against high temperature annealing.

E. Evaluation of STT efficiency

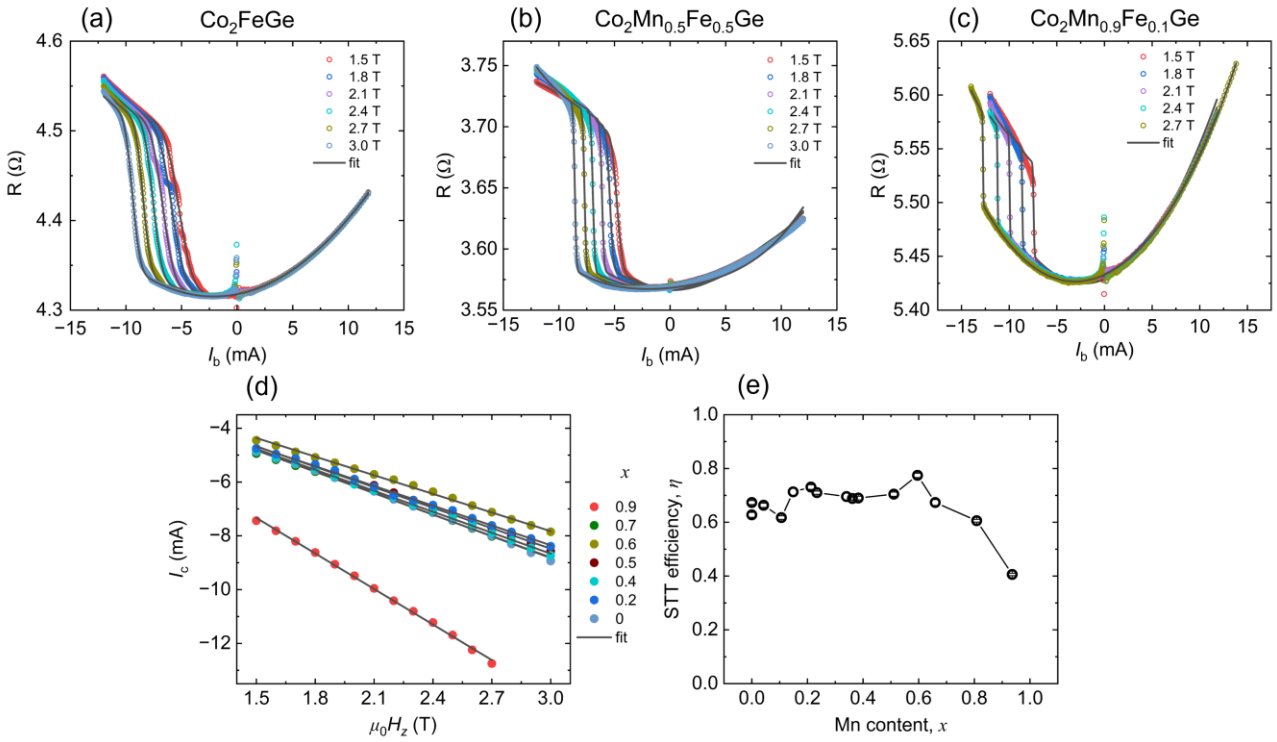

FIG. 7. R-I_b curves at several constant $\mu_0 H_z$ values for the 350°C PA Type-II sample at three different compositions (a) x = 0, (b) x = 0.5, and (c) x = 0.9. (d) Variation of critical current (I_c) with $\mu_0 H_z$ at several CMFG compositions (x = 0, 0.2, 0.4, 0.5, 0.6, 0.7, 0.9) and (e) Variation of STT efficiency (η) with Mn content.

We performed the STT induced magnetization reversal measurements to evaluate the composition dependent STT efficiency for the 350°C PA Type-II sample using devices with circular pillar geometry having designed diameter of 80 nm. Figures 7(a), 7(b) and 7(c) shows several resistance versus bias current (R-I_b) curves measured at constant $\mu_0 H_z$ (magnetic field applied perpendicular to the sample surface) values varying from 1.5 T to 3 T in steps of 0.1 T, for three compositions: x = 0 (Co_2FeGe), x = 0.5 ($Co_2Mn_{0.5}Fe_{0.5}Ge$), and x = 0.9 ($Co_2Mn_{0.9}Fe_{0.1}Ge$), respectively. Sufficiently large $\mu_0 H_z$ (> 1.5 T) was applied to saturate the magnetization of both the FL and SIL parallel to the

magnetic field at zero bias current. For both signs of bias, the R-I_b curves exhibited an overall parabolic increase in R which can be ascribed to the Joule heating. The additional step in R appears on applying sufficiently large negative bias, which corresponds to the reversal of FL (NiFe) magnetization due to the STT from SIL (CMFG). The sign of the bias required for the reversal is as expected for the spin-transfer induced FL reversal. For the applied biased current range, the magnetization reversal of the SIL at positive bias was not observed, due to the large magnetic volume of SIL and low STT efficiency of the NiFe. As observed in the R-I_b curves, the I_b amplitude required to induce the magnetization reversal increases with $\mu_0 H_z$. The value of the required current density(~ 4×10^7 A/cm^2) for magnetization switching is comparable to those reported previously in the CPP-GMR structures[6,58,59].

The R-I_b curves were fitted phenomenologically using the following equation:

$$\mathrm{R} = f(I_\mathrm{b}) + \frac{\Delta\mathrm{R}}{2}\left(1 + \mathrm{erfc}\left(\frac{I_\mathrm{b} - I_\mathrm{c}}{I_\mathrm{width}}\right)\right), \quad (2)$$

where f is a second-order polynomial function representing the R change due to the temperature change, ΔR represents the amount of the R change due to the magnetization reversal, erfc is the error function, I_c corresponds to the I_b value at the center of the R change, and I_width represents the I_b width of the R change covering approximately 85% of the R change. Figure 7(d) shows the change in I_c with $\mu_0 H_z$ for several CMFG compositions. We applied spin transfer torque model, considering that the SIL magnetization is in the +z direction owing to the $\mu_0 H_z$, the FL magnetization rotates near the equator owing to the balance of STT and damping term. The critical current density J_c that satisfies balance between the damping and STT terms is proportional to H_eff and is expressed as:

$$J_\mathrm{c} = \mu_0 \frac{2|e|}{\hbar\eta} \alpha M_\mathrm{s}^\mathrm{FL} d H_\mathrm{eff}. \quad (3)$$

Here d (7 nm) is the thickness of the NiFe FL. M_s^FL (0.9 T) is the saturation magnetization and α

(0.011) is the damping constant of the NiFe determined for the MgO//Cr(5nm)/Ag(5nm)/$Ni_{81}Fe_{19}$(7nm)/Ru(8nm) stack using vibrating sample magnetometer and ferromagnetic resonance measurement. The STT efficiency, η is estimated from the slope of the linear relation between J_c and H_{eff} excluding the effect of the dipolar field from the SIL and demagnetizing field of the FL, which are included in H_{eff}. As observed from the figure 7(d), I_c changes linearly with H_z which is consistent with the model. The STT efficiency is a dimensionless quantity, dependent on the spin polarization of the conduction electron in the FM layers and the relative angle between magnetization directions of the FL and SIL. Slonczewski gave a formula for the η, suitable for the CPP-GMR junctions by considering a free electron model as:

$$\eta = \left[-4 + (1+P)^3(3 + \mathbf{p}\cdot\mathbf{m}_{\text{FL}})/4P^{3/2}\right]^{-1}. \quad (4)$$

$\mathbf{p}$ is a unit vector in the direction of spin polarization of SIL and $\mathbf{m}_{\text{FL}}$ is the unit vector in the direction of FL magnetization. Figure 7(e) shows the η at several CMFG compositions for the Type-III sample. The η exhibits high value ~ 0.6 across the composition range $0 \leq x \leq 0.8$, decline slightly with value reaching close to 0.3 towards the Mn rich (x = 0.9) composition. The drop in η at higher Mn composition could be related to the existence of secondary phases as discussed previously in terms of drop in MR ratio. The high value of η indicates high spin polarization in epitaxially grown CMFG Heusler thin films over a broad composition range.

F. Temperature dependence of MR and STT

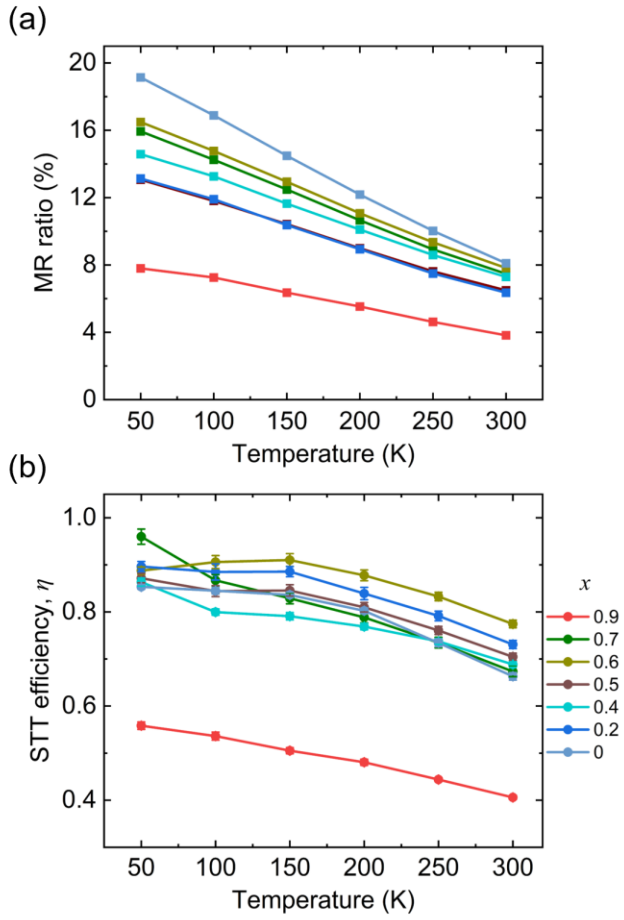

FIG. 8. Temperature dependence of (a) MR ratio and (b) STT efficiency (η) at several $Co_2Mn_xFe_{1-x}Ge$ compositions (x = 0, 0.2, 0.4, 0.5, 0.6, 0.7, 0.9) for the 350°C PA Type-II sample.

We performed the temperature dependent MR and STT measurement for the 350°C PA Type-II sample. Figure 8(a) shows the change in observed MR ratio with measurement temperature at several $Co_2Mn_xFe_{1-x}Ge$ compositions (x=0, 0.2, 0.4, 0.5, 0.6, 0.7, 0.9), calculated from the out-of-plane *R-H* measurements for the CPP-GMR devices. The measurement temperature was varied from 50 K to 300 K in steps of 50 K. Figure 8 (b) shows the variation of STT efficiency with measurement temperature for the same devices as used for the *R-H* measurement. The temperature dependent out-

of-plane MR curves, recorded at different temperature for three different compositions ($x = 0$, $x = 0.5$, and $x = 0.9$) and R-I_b curves at 50K for the same compositions are shown in figure S5 and S6 in the supplementary material, respectively. The increase in MR ratio at low temperature in Heusler alloy based CPP-GMR is understood to be due to increased spin-dependent scattering effect. The temperature dependence of MR ratio ($\Delta R_{50K}/\Delta R_{300K}$) is higher for Fe rich composition (1.93) than Mn rich composition (1.74), indicating that Fe rich composition has a higher spin asymmetry of scattering of the conduction electrons than Mn rich composition at low temperatures[40]. MR ratios show large temperature dependence in several studies where the MR increases by a factor of two or three from room temperature to low temperature[3,5,13]. The STT efficiency also improves with decreasing temperature, changes more gradually at lower temperatures (200 K-50 K) as compared to the change in MR% with temperature.

G. Discussion and comparison with other CPP-GMR structures

The MR and STT are the characteristic magnetotransport phenomenon closely related to each other through the spin polarization of charge carriers. In a FM/non-magnet/FM structure, the MR is related to the component in the interlayer which is parallel to the magnetization of the second layer and the STT is related to the absorption of transverse component of the spin polarized current (generated by spin polarization of SIL layer) by the free FM layer. We recently explained the qualitative agreement between the MR and the STT response in CPP GMR devices fabricated from NiFe(10nm)/Co_xFe_{1-x}(5nm)/Cu(3nm)/NiFe(5nm) GMR stacks containing composition-gradient Co_xFe_{1-x} ($0 \leq x \leq 1$) layer in the SIL. MR and STT were found to be correlated to the bulk spin polarization of the SIL[32]. There we observed maximum MR ratio ~2.8% and STT efficiency ~ 0.4 for the composition range $0.3 \leq x \leq 0.65$ in Co_xFe_{1-x}. For the present study comprising CMFG Heusler films based CPP-GMR devices, we observed approximately 2-fold increment in MR ratio along with 75% enhancement in the STT efficiency as compared to Co_xFe_{1-x} ($0 \leq x \leq 1$) film studied previously, highlighting the higher spin

polarization in the CMFG Heusler thin films. We obtained large MR ratio ~ 38 % at relatively low annealing temperature of 250°C for the Mn-rich CMFG composition ($x = 0.85$). The MR ratio exhibits 1.6 fold increase when x is varied from 0 to 0.85 in CMFG for the 250°C PA sample. Although the Co/Ge ratio changes ~16% from CFG to CMG side in the present study, Ref. [35] reports that a 15% change in Co/Ge ratio in CMFG led to a ~ 1.1-fold change in the MR ratio. This suggests that the Mn/Fe ratio plays a more significant role in enhancing the MR ratio. The larger MR ratio > 45% along with high STT efficiency ~0.6 was obtained for a broad composition range of $0.2 \leq x \leq 0.7$ at 350°C annealing temperature. The optimal composition range for the high MR changed with annealing temperature. Mn being more prone to diffusion, Fe rich FM electrode composition was found to be more stable against diffusion at the interface between FM electrode and spacer at higher annealing temperature. The large MR ratio obtained over broad composition range ($0.2 \leq x \leq 0.7$) for the 350 °C annealed type-I sample having $L2_1$ ordered CMFG electrodes is in qualitative agreement with the large values of calculated P_{sp} (> 95 %) over the broad composition range ($0.3 \leq x \leq 1$). Although experimental and theoretical results are consistent in that the MR ratio and P_{sp} show a decrease in CFG side, decrease in the MR ratio is rather gentle in contrast to the loss of half-metallic character in the calculated P_{sp}, which can be attributed to the following reason. The GGA method is insufficient for systems with well-localized *d*-electron orbitals because the GGA method tends to delocalize these electrons, leading to an inaccurate representation of the electron correlation. Consequently, incorporating an on-site Coulomb interaction (U), as in the GGA + U approach[60,61] is recommended. Previous studies argued the requirement of U to obtain more accurate DOS in Co-based Heusler alloy[62]. Addressing this limitation in future work could improve the alignment between theory and experiment.

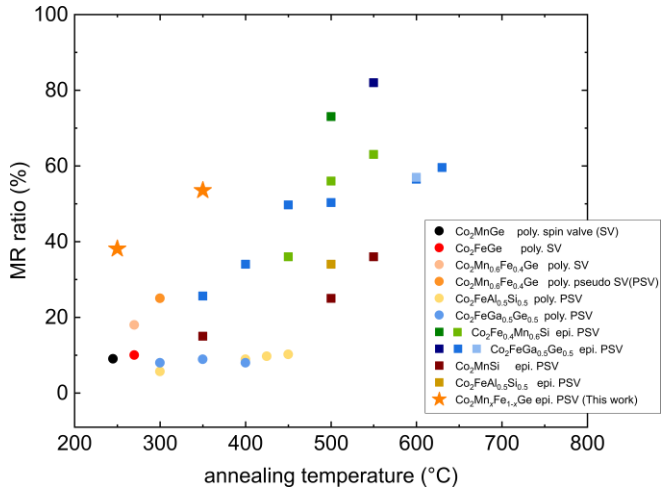

FIG. 9. Intrinsic MR ratio v/s annealing temperature for all-metal CPP-GMR devices containing different Heusler thin film as FM electrodes[3,7,55,8–11,13,36–38]. The symbol color represents the types of Heusler materials, and the circular and square symbols represent the data for polycrystalline (poly.) and epitaxial (epi.) CPP-GMR devices. The data from different studies on the same Heusler material are shown by the same color with different shade. SV (PSV) in the legend stands for spin valve (pseudo spin valve) CPP-GMR devices. The star symbols show the present data for the CPP-GMR devices containing composition-gradient CMFG Heusler thin films.

Figure 9 shows the intrinsic MR ratio v/s annealing temperature for the present CPP-GMR stacks containing composition-gradient CMFG films, shown by star symbols, in comparison to all-metal spin valves and pseudo spin valves devices containing polycrystalline CMG, CFG, $Co_2Mn_{0.6}Fe_{0.4}Ge$, CFGG and CFAS Heusler thin films shown by circular symbols and epitaxial CMS, CFAS, CMFS and CFGG Heusler thin films shown by square symbols, as FM electrodes[3,7,55,8–11,13,36–38]. Compared to the literature values, we achieved highest MR ratio ~ 38% and 53% at x = 0.85 and x = 0.13, respectively in the present CMFG Heusler based CPP-GMR devices at low annealing temperature of 250°C and 350°C, respectively. The Heusler alloy based CPP-GMR devices showing large MR ratio (>30%), often require high temperature annealing more than 450°C to achieve good magneto transport properties. For practical applications, for example in the read head sensor's fabrication

process, the maximum applicable annealing temperature could be 350°C[12]. The large MR ratio obtained at lower annealing temperature in the present study highlights the advantage of using CMFG Heusler thin films in the CPP-GMR devices for the future read head sensor applications.

IV. CONCLUSION

We fabricated high performance CPP-GMR devices from the GMR stacks containing composition-gradient $Co_2Mn_xFe_{1-x}Ge$ ($0 \leq x \leq 1$) film by high throughput and detailed composition optimization method. The combinatorially sputtered composition-gradient film and local measurements enabled efficient compositional optimization at fine composition interval. The XRD measurement conducted at several positions on the GMR stacks with different compositions revealed the epitaxial and largely single-phase structure throughout the composition range and improvement in atomic ordering with annealing temperature. The CPP-GMR devices fabricated from the stacks annealed at 250°C exhibit clear composition dependence of MR with a maximum of change in ΔRA ~ 5 mΩ μm^2 and MR ratio ~ 38 % in the Mn-rich region of x = 0.85. The MR ratio was further enhanced with increasing annealing temperature to 350°C and we observed maximum MR ratio close to ~ 45% (ΔRA ~ 8 mΩ μm^2) along with high STT efficiency ~ 0.6 over a broad composition range $0.2 \leq x \leq 0.7$. The optimal composition range shifted to lower x with increasing annealing temperature as the stability of the interface between FM electrode and spacer was changed and higher for Fe rich composition. We achieved record high MR for the all-metal CPP-GMR devices at low annealing temperature of 250°C by the present composition optimization method. The results provide comprehensive guidance on the composition optimization to obtain large MR ratio and high STT efficiency in the CPP-GMR devices using $Co_2Mn_xFe_{1-x}Ge$ at lower process temperature.

SUPPLEMENTARY MATERIAL

See the supplementary material for details on the change in observed MR ratio and ΔRA with Mn content in CMFG for the as-deposited, 250°C and 350°C PA Type-I sample; in-plane *R*-*H* curves for the as-deposited, 250 °C and 350 °C PA Type-I samples at three different compositions viz. Co_2FeGe, $Co_2Mn_{0.5}Fe_{0.5}Ge$ and Co_2MnGe; in-plane *R*-*H* curves for the 350 °C PA Type-II sample at three different compositions viz. Co_2FeGe, $Co_2Mn_{0.5}Fe_{0.5}Ge$ and $Co_2Mn_{0.9}Ge_{0.1}$; change in observed MR ratio and ΔRA with Mn content in CMFG for the 350°C PA Type-II sample; out-of-plane MR curves in the temperature range of 300 K to 50 K for the 350°C PA Type-II sample at three different compositions viz. Co_2FeGe, $Co_2Mn_{0.5}Fe_{0.5}Ge$ and $Co_2Mn_{0.9}Fe_{0.1}Ge$; R-I_b curves at 50 K for several constant $\mu_0 H_z$ values for the 350°C PA Type-II sample at three different compositions viz. Co_2FeGe, $Co_2Mn_{0.5}Fe_{0.5}Ge$ and $Co_2Mn_{0.9}Fe_{0.1}Ge$; and the table showing the summary of MR properties studied at room temperature for the CPP-GMR devices containing $Co_2Mn_xFe_{1-x}Ge$ ($0 \leq x \leq 1$) Heusler as ferromagnetic layer electrode with metallic spacers, which includes Refs. [54-57].

ACKNOWLEDGEMENTS

This work was supported by the Advanced Storage Research Consortium (ASRC), JST CREST Grant No. JPMJCR21O1, MEXT Program: Data Creation and Utilization-Type Material Research and Development Project Grant Number JPMXP1122715503, and MEXT Initiative to Establish Next-generation Novel Integrated Circuits Centers (X-NICS) grant number JPJ011438.

AUTHOR DECLARATION

Conflict of Interest

The authors have no conflicts to disclose.

Author Contributions

Vineet Barwal: Data curation (equal); Formal analysis (equal); Investigation (equal); Visualization (equal); Writing - original draft (equal); Writing - review and editing (equal). **Hirofumi Suto**: Conceptualization (equal); Formal analysis (equal); Methodology (equal); Project Administration (equal); Resources (equal); Supervision (equal); Writing-review and editing (equal). **Ryo Toyama**: Formal analysis (supporting); Investigation (supporting); Writing-review and editing (supporting). **Kodchakorn Simalaotao**: Formal analysis (supporting); Investigation (supporting); Writing-review and editing (supporting). **Taisuke Sasaki**: Investigation (equal); Writing-review and editing (supporting). **Yoshio Miura**: Formal analysis (supporting); Investigation (supporting); Writing-review and editing (supporting). **Yuya Sakuraba**: Conceptualization (equal); Project Administration (equal); Resources (equal); Supervision (equal); Writing-review and editing (equal).

DATA AVAILABILITY

The data that support the findings of this study are available within the article and its supplementary material.

REFERENCES

[1] K. Elphick, W. Frost, M. Samiepour, T. Kubota, K. Takanashi, H. Sukegawa, S. Mitani, and A. Hirohata, Sci. Technol. Adv. Mater. **22**, 235 (2021).

[2] A. Hirohata and D.C. Lloyd, MRS Bull. **47**, 593 (2022).

[3] Y. Sakuraba, K. Izumi, T. Iwase, S. Bosu, K. Saito, K. Takanashi, Y. Miura, K. Futatsukawa, K. Abe, and M. Shirai, Phys. Rev. B - Condens. Matter Mater. Phys. **82**, 094444 (2010).

[4] J. Sato, M. Oogane, H. Naganuma, and Y. Ando, Appl. Phys. Express **4**, 113005 (2011).

[5] Y. Sakuraba, M. Ueda, Y. Miura, K. Sato, S. Bosu, K. Saito, M. Shirai, T.J. Konno, and K. Takanashi, Appl. Phys. Lett. **101**, 252408 (2012).

[6] H. Narisawa, T. Kubota, and K. Takanashi, Appl. Phys. Express **8**, 063008 (2015).

[7] T. Kubota, Y. Ina, Z. Wen, H. Narisawa, and K. Takanashi, Phys. Rev. Mater. **1**, 044402 (2017).

[8] Z. Wen, T. Kubota, Y. Ina, and K. Takanashi, Appl. Phys. Lett. **110**, 102401 (2017).

[9] T.M. Nakatani, T. Furubayashi, S. Kasai, H. Sukegawa, Y.K. Takahashi, S. Mitani, and K. Hono, Appl. Phys. Lett. **96**, 212501 (2010).

[10] S. Li, Y.K. Takahashi, T. Furubayashi, and K. Hono, Appl. Phys. Lett. **103**, 042405 (2013).

[11] Y. Du, T. Furubayashi, T.T. Sasaki, Y. Sakuraba, Y.K. Takahashi, and K. Hono, Appl. Phys. Lett. **107**, 112405 (2015).

[12] T. Nakatani, Z. Gao, and K. Hono, MRS Bull. **43**, 106 (2018).

[13] J.W. Jung, Y. Sakuraba, T.T. Sasaki, Y. Miura, and K. Hono, Appl. Phys. Lett. **108**, 102408 (2016).

[14] Y.K. Takahashi, A. Srinivasan, B. Varaprasad, A. Rajanikanth, N. Hase, T.M. Nakatani, S. Kasai, T. Furubayashi, and K. Hono, Appl. Phys. Lett. **98**, 152501 (2011).

[15] B. Büker, J. Jung, T. Sasaki, Y. Sakuraba, Y. Miura, T. Nakatani, A. Hütten, and K. Hono, Phys. Rev. B **103**, L140405 (2021).

[16] T. Kubota, Z. Wen, and K. Takanashi, J. Magn. Magn. Mater. **492**, 165667 (2019).

[17] Y. Chikaso, M. Inoue, T. Tanimoto, K. Kikuchi, M. Yamanouchi, T. Uemura, K. Inubushi, K. Nakada, H. Shinya, and M. Shirai, J. Phys. D. Appl. Phys. **55**, 345003 (2022).

[18] Z. Wen, H. Sukegawa, S. Kasai, K. Inomata, and S. Mitani, Phys. Rev. Appl. **2**, 024009 (2014).

[19] J. Zhang, T. Phung, A. Pushp, Y. Ferrante, J. Jeong, C. Rettner, B.P. Hughes, S.H. Yang, Y. Jiang, and S.S.P. Parkin, Appl. Phys. Lett. **110**, 172403 (2017).

[20] A. V. Khvalkovskiy, D. Apalkov, S. Watts, R. Chepulskii, R.S. Beach, A. Ong, X. Tang, A. Driskill-Smith, W.H. Butler, P.B. Visscher, D. Lottis, E. Chen, V. Nikitin, and M. Krounbi, J. Phys. D. Appl. Phys. **46**, 139601 (2013).

[21] S. Okamoto, N. Kikuchi, M. Furuta, O. Kitakami, and T. Shimatsu, J. Phys. D. Appl. Phys. **48**, 353001 (2015).

[22] W. Zhou, H. Sepehri-Amin, T. Taniguchi, S. Tamaru, Y. Sakuraba, S. Kasai, H. Kubota, and K. Hono, Appl. Phys. Lett. **114**, 172403 (2019).

[23] M. Takagishi, N. Narita, H. Iwasaki, H. Suto, T. Maeda, and A. Takeo, IEEE Trans. Magn. **57**, 3300106 (2021).

[24] H. Suto, M. Takagishi, N. Narita, H. Iwasaki, T. Nagasawa, G. Koizumi, A. Takeo, and T. Maeda, J. Appl. Phys. **129**, 103901 (2021).

[25] R. Toyama, V.K. Kushwaha, T.T. Sasaki, Y. Iwasaki, T. Nakatani, and Y. Sakuraba, APL Mater. **11**, 101127 (2023).

[26] Y. Sakuraba, S. Kokado, Y. Hirayama, T. Furubayashi, H. Sukegawa, S. Li, Y.K. Takahashi, and K. Hono, Appl. Phys. Lett. **104**, 172407 (2014).

[27] C. Guillemard, W. Zhang, G. Malinowski, C. de Melo, J. Gorchon, S. Petit-Watelot, J. Ghanbaja, S. Mangin, P. Le Fèvre, F. Bertran, and S. Andrieu, Adv. Mater. **32**, 1908357 (2020).

[28] M. Inoue, B. Hu, K. Moges, K. Inubushi, K. Nakada, M. Yamamoto, and T. Uemura, Appl. Phys. Lett. **111**, 082403 (2017).

[29] S. Li, Y.K. Takahashi, Y. Sakuraba, N. Tsuji, H. Tajiri, Y. Miura, J. Chen, T. Furubayashi, and K. Hono, Appl. Phys. Lett. **108**, 122404 (2016).

[30] A. Frisk, M. Ahlberg, G. Muscas, S. George, R. Johansson, W. Klysubun, P.E. Jönsson, and G. Andersson, Phys. Rev. Mater. **3**, 074403 (2019).

[31] H. Masuda, R. Modak, T. Seki, K. Uchida, Y.-C. Lau, Y. Sakuraba, R. Iguchi, and K. Takanashi, Commun. Mater. **1**, 75 (2020).

[32] V. Barwal, H. Suto, T. Taniguchi, and Y. Sakuraba, Sci. Technol. Adv. Mater. Methods **3**(1), 2286944 (2023).

[33] S. Picozzi, A. Continenza, and A.J. Freeman, Phys. Rev. B - Condens. Matter Mater. Phys. **69**, 094423 (2004).

[34] Y. Miura, K. Nagao, and M. Shirai, Phys. Rev. B - Condens. Matter Phys. **69**, 144413 (2004).

[35] T. Nakatani, S. Li, Y. Sakuraba, T. Furubayashi, and K. Hono, IEEE Trans. Magn. **54**, 3300211 (2018).

[36] T. Nakatani, G. Mihajlović, J.C. Read, Y.S. Choi, and J.R. Childress, Appl. Phys. Express **8**, 093003 (2015).

[37] Y.S. Choi, T. Nakatani, J.C. Read, M.J. Carey, D.A. Stewart, and J.R. Childress, Appl. Phys. Express **10**, 013006 (2017).

[38] S. Li, T. Nakatani, K. Masuda, Y. Sakuraba, X.D. Xu, T.T. Sasaki, H. Tajiri, Y. Miura, T. Furubayashi, and K. Hono, Acta Mater. **142**, 49 (2018).

[39] T. Nakatani, S.K. Narayananellore, L.S.R. Kumara, H. Tajiri, Y. Sakuraba, and K. Hono, Scr. Mater. **189**, 63 (2020).

[40] M.R. Page, T.M. Nakatani, D.A. Stewart, B.R. York, J.C. Read, Y.-S. Choi, and J.R. Childress, J. Appl. Phys. **119**, 153903 (2016).

[41] R. Toyama, S. Kokado, K. Masuda, Z. Li, V.K. Kushwaha, T.T. Sasaki, L.S.R. Kumara, T. Koganezawa, H. Tajiri, T. Yamazaki, M. Kotsugi, Y. Iwasaki, and Y. Sakuraba, Phys. Rev. Mater. **7**, 084401 (2023).

[42] R. Toyama, W. Zhou, and Y. Sakuraba, Phys. Rev. B **109**(1), 054415 (2024).

[43] H. Suto, T. Nakatani, N. Asam, H. Iwasaki, and Y. Sakuraba, Appl. Phys. Express **16**, 013003 (2023).

[44] B. Balke, S. Wurmehl, G.H. Fecher, C. Felser, M.C.M. Alves, F. Bernardi, and J. Morais, Appl. Phys. Lett. **90**, 172501(2007).

[45] P.J. Webster and K.R.A. Ziebeck, J. Phys. Chem. Solids **34**, 1647 (1973).

[46] J.P. Perdew, K. Burke, and M. Ernzerhof, Phys. Rev. Lett. **77**, 3865 (1996).

588 [47] G. Kresse and J. Hafner, Phys. Rev. B **47**, 558 (1993).

589 [48] G. Kresse and J. Furthmüller, Comput. Mater. Sci. **6**, 15 (1996).

590 [49] P.E. Blöchl, Phys. Rev. B **50**, 17953 (1994).

591 [50] G. Kresse and D. Joubert, Phys. Rev. B **59**, 1758 (1999).

592 [51] L. Bellaiche and D. Vanderbilt, Phys. Rev. B **61**, 7877 (2000).

593 [52] J.D. Pack and H.J. Monkhorst, Phys. Rev. B **16**, 1748 (1977).

594 [53] Z. Chen, Y. Sakuraba, Y. Miura, Z. Li, T. Sasaki, H. Suto, V.K. Kushwaha, T. Nakatani, S. Mitani,
595 and K. Hono, J. Appl. Phys. **132**, 183902 (2022).

596 [54] K. Nikolaev, P. Kolbo, T. Pokhil, X. Peng, Y. Chen, T. Ambrose, and O. Mryasov, Appl. Phys.
597 Lett. **94**, 222501 (2009).

598 [55] M.J. Carey, S. Maat, S. Chandrashekariaih, J.A. Katine, W. Chen, B. York, and J.R. Childress, J.
599 Appl. Phys. **109**, 093912 (2011).

600 [56] T.P. Ginley, J.A. Borchers, B.J. Kirby, C.L. Dennis, M.J. Carey, and J.R. Childress, J. Appl. Phys.
601 **109**,07B110 (2011).

602 [57] H.S. Goripati, T. Furubayashi, Y.K. Takahashi, and K. Hono, J. Appl. Phys. **113**, 043901 (2013).

603 [58] J.A. Katine, F.J. Albert, R.A. Buhrman, E.B. Myers, and D.C. Ralph, Phys. Rev. Lett. **84**, 3149
604 (2000).

605 [59] G. Mihajlović, T.M. Nakatani, N. Smith, J.C. Read, Y.S. Choi, H.W. Tseng, and J.R. Childress,
606 IEEE Magn. Lett. **6**, 3001104 (2015).

607 [60] B. Balke, G.H. Fecher, H.C. Kandpal, C. Felser, K. Kobayashi, E. Ikenaga, J.-J. Kim, and S. Ueda,
608 Phys. Rev. B **74**, 104405 (2006).

609 [61] K. Nawa and Y. Miura, RSC Adv. **9**, 30462 (2019).

610 [62] K. Sumida, Y. Fujita, W. Zhou, K. Masuda, I. Kawasaki, S. Fujimori, A. Kimura, and Y. Sakuraba,
611 Phys. Rev. B **108**, L241101 (2023).

612

613

Supplementary Material

MR analysis for the Type-I sample

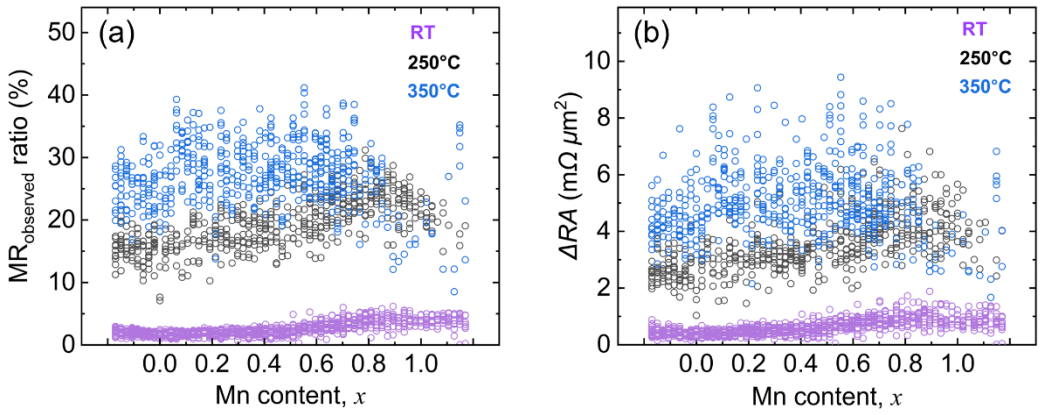

FIG. S1. Change in (a) observed MR ratio and (b) *ΔRA* with Mn content in CMFG for the as-deposited, 250°C and 350°C PA Type-I sample.

Figures S1(a) and S1(b) show the change in observed magnetoresistance (MR) ratio and change in resistance area product (*ΔRA*) with Mn content for the as-deposited, 250°C and 350°C PA Type-I sample. The change in observed MR ratio and *ΔRA* with Mn content is consistent with the change in intrinsic MR ratio with Mn content, as shown in the main manuscript. For the 250°C PA sample, we can see an enhancement in MR% around $x = 0.85$. The observed MR ratio reaches to a maximum value of around 35% for 350°C PA in a broad composition range ($0.2 \leq x \leq 0.7$).

623 ***R-H* curves for Type-I sample**

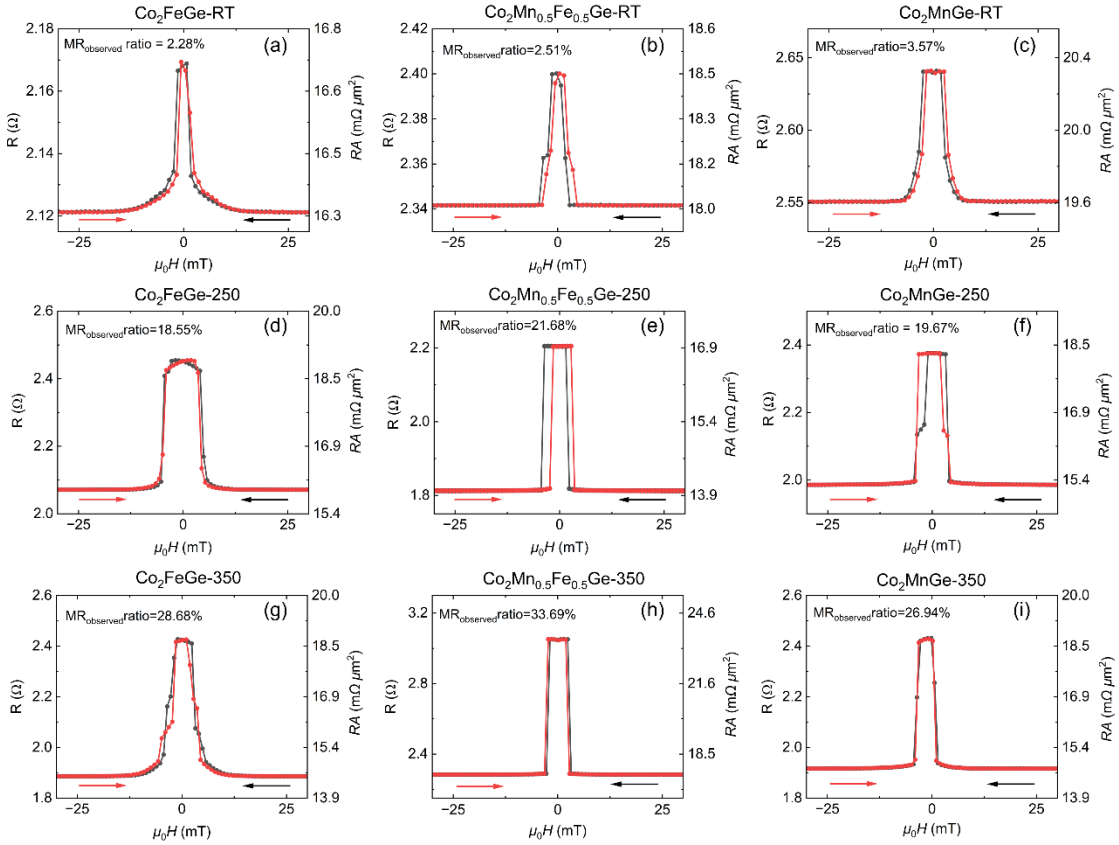

FIG. S2. In-plane *R-H* curves for the as-deposited, 250 °C and 350 °C PA Type-I samples at three different compositions viz. Co_2FeGe, $Co_2Mn_{0.5}Fe_{0.5}Ge$ and Co_2MnGe.

624 Figure S2 shows the in-plane *R-H* curves for the as-deposited, 250 °C and 350 °C PA Type-I samples at
625 three different compositions viz. Co_2FeGe, $Co_2Mn_{0.5}Fe_{0.5}Ge$ and $Co_2Mn_{0.9}Ge_{0.1}$.

626

_R-H_ curves for Type-II sample

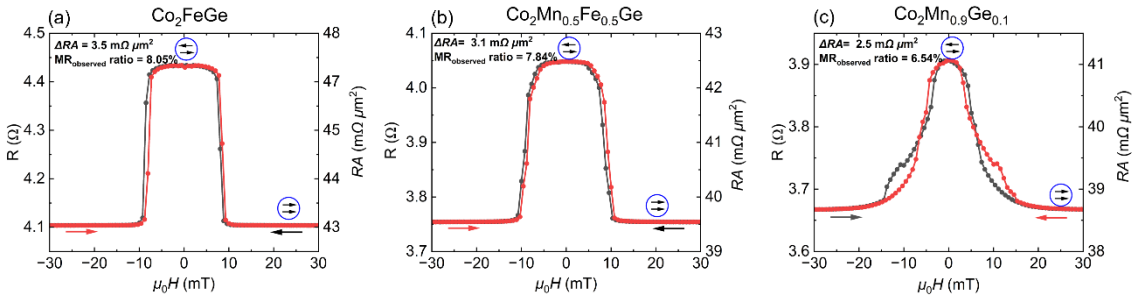

FIG. S3. In-plane *R-H* curves for the 350 °C PA Type-II sample at three different compositions viz. Co_2FeGe, $Co_2Mn_{0.5}Fe_{0.5}Ge$ and $Co_2Mn_{0.9}Ge_{0.1}$.

Figure S3 shows the in-plane *R-H* curves for the 350 °C PA Type-II sample at three different compositions viz. Co_2FeGe, $Co_2Mn_{0.5}Fe_{0.5}Ge$ and $Co_2Mn_{0.9}Ge_{0.1}$.

MR analysis for Type-II sample

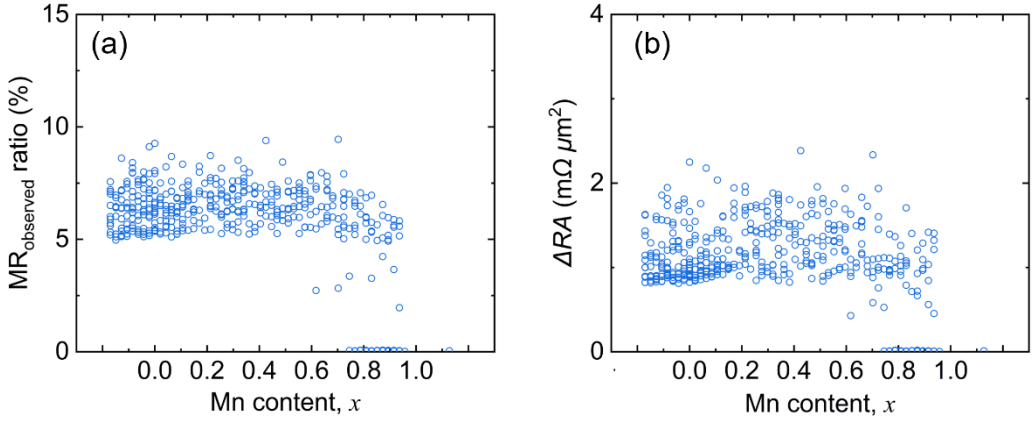

FIG. S4. Change in (a) observed MR ratio and (b) *ΔRA* with Mn content in CMFG for the 350°C PA Type-II sample.

Figures S4(a) and S4(b) show the change in observed MR ratio and *ΔRA* with Mn content for the 350°C PA Type-II sample. The MR ratio and *ΔRA* do not change much with Mn content, except for the drop around higher Mn concentration, similar to the 350 °C PA Type-I sample. The MR ratio and *ΔRA* values reduce by a factor of 0.25 for the Type-II sample as compared to Type-I sample. Change in *ΔRA* was

calculated from the MR measurements using the designed device cross sectional area. The large distribution in ΔRA for the 350 °C PA samples, is due to increased diffusion at the interface at higher annealing temperature.

MR curves for Type-II sample at different measurement temperatures

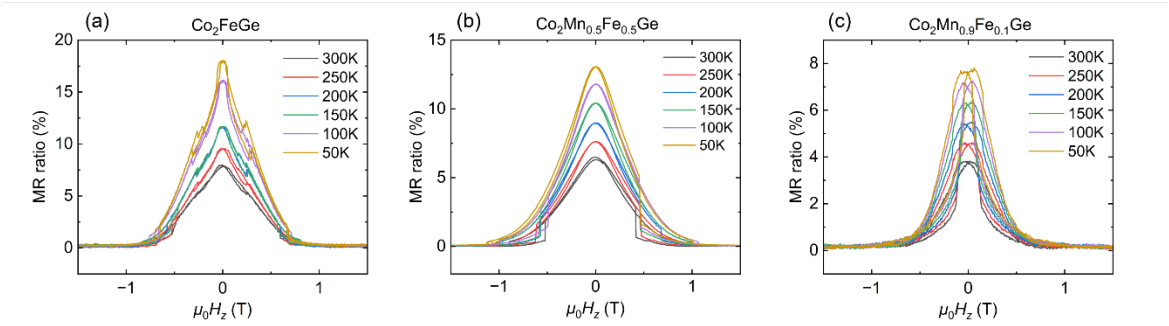

FIG. S5. Out-of-plane MR curves in the temperature range of 300 K to 50 K for the 350°C PA Type-II sample at three different compositions (a) Co_2FeGe, (b) $Co_2Mn_{0.5}Fe_{0.5}Ge$ and (c) $Co_2Mn_{0.9}Fe_{0.1}Ge$.

Figures S5 (a), (b) and (c) show the out-of-plane MR curves at different temperatures (50 K, 100 K, 150 K, 200 K, 250 K and 300 K) for the 350°C PA Type-II sample at three different compositions (Co_2FeGe, $Co_2Mn_{0.5}Fe_{0.5}Ge$ and $Co_2Mn_{0.9}Fe_{0.1}Ge$). The MR ratio increased more than 2.5 times upon decreasing the temperature from 300 K to 50 K.

Magnetization reversal curves at 50K for Type-II sample

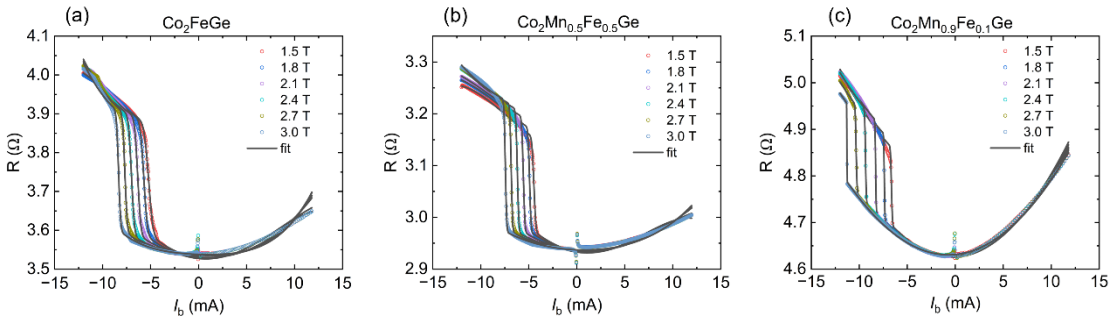

FIG. S6. R-I_b curves at 50 K for several constant $\mu_0 H_z$ values for the 350°C PA Type-II sample at three different compositions (a) Co_2FeGe, (b) $Co_2Mn_{0.5}Fe_{0.5}Ge$ and (c) $Co_2Mn_{0.9}Fe_{0.1}Ge$.

Figures S6 (a), (b) and (c) show the R-I_b curves at 50 K for several constant $\mu_0 H_z$ values (1.5 T, 1.8 T, 2.1 T, 2.4 T, 2.7 T and 3 T) for the 350°C PA Type-II sample for three different compositions viz. Co_2FeGe, $Co_2Mn_{0.5}Fe_{0.5}Ge$ and $Co_2Mn_{0.9}Fe_{0.1}Ge$. STT efficiency increased by factor of ~ 1.4 upon decreasing the temperature from 300 K to 50 K.

Summary of MR study on $Co_2Mn_xFe_{1-x}Ge$ ($0 \leq x \leq 1$) [CMFG] Heusler based CPP-GMR devices

Table S1. Summary of MR properties studied at room temperature for CPP-GMR devices containing $Co_2Mn_xFe_{1-x}Ge$ ($0 \leq x \leq 1$) [CMFG] Heusler as ferromagnetic layer electrode with metallic spacers. The epitaxially grown stacks are indicated by acronym "epi." and polycrystalline stacks are indicated by acronym "poly.". Numbers in the parentheses indicates layer thickness in nm. PSVs are the pseudo spin valves without any pinned layer and SVs means spin valves with pinned layer. RT denotes room temperature meaning no annealing was done for the CPP-GMR stacks.

CPP-GMR stacking structure	MR ratio (%)	ΔRA (mΩ μm²)	Annealing Temperature (°C)	Ref.
Co_2MnGe (CMG)				
Seed layer/IrMn/CoFe/Ru/CMG(3.6)/Rh_2CuSn(2.2)/CMG(3.6) /capping layer **poly. SV**	6.7	4	250	[1]
Seed layer/IrMn(7)/$Co_{65}Fe_{35}$(4)/Ru(0.8)/$Co_{90}Fe_{10}$(0.6)/CMG(4) /$Co_{90}Fe_{10}$(0.6)/Cu(8)/$Co_{90}Fe_{10}$(0.6)/CMG(4)/ $Co_{90}Fe_{10}$(0.6)/Cu(8)/$Co_{90}Fe_{10}$(0.6)/CMG(4)/$Co_{90}Fe_{10}$(0.6) /capping layer **poly. SV**	9	6	245	[2]
Seed layer/CMG(8)/Cu(5)/$Co_{50}Fe_{50}$(0.5)/CMG(4)/$Co_{50}Fe_{50}$(1)/ IrMn(6)/Ru(12)/capping layer **poly. SV**	-	2.6	245	[3]
Seed layer/$Co_{50}Fe_{50}$(0.5)/CMG(8)/$Co_{50}Fe_{50}$(0.5)/Cu(5)/$Co_{50}Fe_{50}$(0.5)/CMG(4)/$Co_{50}Fe_{50}$(1)/IrMn(6)/Ru(12)/capping layer **poly. SV**	-	3.2		
Co_2FeGe (CFG)				
Seed layer/CFG(10)/Ag(5)/CFG(10)/capping layer **epi. PSV**	-	4	300	[4]
Seed layer/Ru(2)/IrMn(6)/$Co_{50}Fe_{50}$(1)/CFG(4)/$Co_{50}Fe_{50}$(0.5)/ Ag(3.5)/$Co_{50}Fe_{50}$(0.5)/CFG(4)/$Co_{50}Fe_{50}$(1)/capping layer **poly. SV**	10	-	270/280	[5]
$Co_2Mn_xFe_{1-x}Ge$ (CMFG)				
Seed layer/IrMn(6)/$Co_{50}Fe_{50}$(2.7)/Ru(0.8)/$Co_{50}Fe_{50}$(0.7)/ CMFG(6.5)/$Co_{50}Fe_{50}$(0.5)/$Ag_{90}Sn_{10}$(2.5)/$Co_{50}Fe_{50}$(0.5) /CMFG(6.5)/capping layer x = 0.6 **poly. SV**	15	-	270/280	[5]
Seed layer/IrMn(5)/$Co_{50}Fe_{50}$(2.6)/Ru(0.8)/$Co_{50}Fe_{50}$(0.7)/ CoFeBTa(0.6)/CMFG(2.5)/$Co_{50}Fe_{50}$(0.2)/$Ag_{90}Sn_{10}$(4)/ $Co_{50}Fe_{50}$(0.2)/CMFG(4)/$Co_{50}Fe_{50}$(1)/Ru(0.8)/ $Co_{50}Fe_{50}$(1.2)/capping layer x = 1, 0.9, 0.8, 0.6 **poly. SV**	13	6	270	[6]
Seed layer/IrMn(5)/Co(0.4)/$Co_{50}Fe_{50}$(0.8)/ $(Co_{40}Fe_{40}B_{20})_{0.93}Ta_{0.07}$(0.9)/CMFG(2.5)/$Co_{50}Fe_{50}$(0.2)/ $Ag_{90}Sn_{10}$(3.5)/$Co_{50}Fe_{50}$(0.2)/CMFG(4)/capping layer x = 0.6 **poly. SV**	18	8	270	[7]
Seed layer/CMFG(10)/Ag(5)/CMFG(10)/capping layer x = 0.6 **epi. PSV**	-	9.5	400	[8]
Seed layer/CMFG(5)/$Ag_{90}Sn_{10}$(4)/CMFG(5)/capping layer	-	7.5	300	

x = 0.6 **poly. PSV**				
Seed layer/IrMn(6)/$Co_{50}Fe_{50}$(1)/$(Co_{40}Fe_{40}B_{20})_{0.93}Ta_{0.07}$(0.8)/ CMFG(5)/$Co_{50}Fe_{50}$(0.4)/$Ag_{90}Sn_{10}$(3.5)/$Co_{50}Fe_{50}$(0.4)/ CMFG(5)/$Co_{50}Fe_{50}$(1)/capping layer x = 0.6 **poly. SV**	16	-	300	
Seed layer/IrMn(6)/$Co_{50}Fe_{50}$(3)/Ru(0.8)/$Co_{50}Fe_{50}$(0.6)/ $(Co_{40}Fe_{40}B_{20})_{0.93}Ta_{0.07}$(0.8)/CMFG(3)/$Co_{50}Fe_{50}$(0.4)/$Ag_{90}$ Sn_{10}(3.5)/$Co_{50}Fe_{50}$(0.4)/CMFG(4)/$Co_{50}Fe_{50}$(1)/capping layer x = 0.6 **poly. SV**	14	4	280	
Seed layer/$(Co_{40}Fe_{40}B_{20})_{0.93}Ta_{0.07}$(1.2)/CMFG(5)/$Co_{50}Fe_{50}$(0.4) /$Ag_{90}Sn_{10}$(4)/$Co_{50}Fe_{50}$(0.4)/CMFG(5)/$Co_{50}Fe_{50}$(1)/ capping layer x = 0.6 **poly. PSV**	25	7.5	300	[9]
Seed layer/$(Co_{40}Fe_{40}B_{20})_{0.93}Ta_{0.07}$(0.6)/CMFG(4)/$Co_{50}Fe_{50}$(0.4) /$Ag_{90}Sn_{10}$(3.5)/$Co_{50}Fe_{50}$(0.4)/CMFG(5)/$Co_{50}Fe_{50}$(1)/ capping layer x = 0.6 **poly. PSV**	17.8	6	300	[10]
Seed layer/CMFG(7)/$Ag_{90}Sn_{10}$(5)/CMFG(7)/capping layer $0.2 \leq x \leq 0.7$ **epi.PSV**	35-45	4-8	350	Present case
Seed layer/CMFG(7)/$Ag_{90}Sn_{10}$(5)/CMFG(7)/capping layer x = 0.85 **epi. PSV**	35	5	250	
Seed layer/CMFG(7)/$Ag_{90}Sn_{10}$(5)/CMFG(7)/capping layer $0.8 \leq x \leq 1$ **epi. PSV**	3-6	0.6-1.5	RT	

References

[1] K. Nikolaev, P. Kolbo, T. Pokhil, X. Peng, Y. Chen, T. Ambrose, and O. Mryasov, Appl. Phys. Lett. **94**, 222501 (2009).

[2] M.J. Carey, S. Maat, S. Chandrashekariaih, J.A. Katine, W. Chen, B. York, and J.R. Childress, J. Appl. Phys. **109**, 093912 (2011).

[3] T.P. Ginley, J.A. Borchers, B.J. Kirby, C.L. Dennis, M.J. Carey, and J.R. Childress, J. Appl. Phys. **109**, (2011).

[4] H.S. Goripati, T. Furubayashi, Y.K. Takahashi, and K. Hono, J. Appl. Phys. **113**, 043901 (2013).

[5] T. Nakatani, G. Mihajlović, J.C. Read, Y.S. Choi, and J.R. Childress, Appl. Phys. Express **8**, 093003 (2015).

[6] M.R. Page, T.M. Nakatani, D.A. Stewart, B.R. York, J.C. Read, Y.-S. Choi, and J.R. Childress, J. Appl. Phys. **119**, 153903 (2016).

[7] Y.S. Choi, T. Nakatani, J.C. Read, M.J. Carey, D.A. Stewart, and J.R. Childress, Appl. Phys. Express **10**, 013006 (2017).

[8] T. Nakatani, S. Li, Y. Sakuraba, T. Furubayashi, and K. Hono, IEEE Trans. Magn. **54**, 3300211 (2018).

[9] S. Li, T. Nakatani, K. Masuda, Y. Sakuraba, X.D. Xu, T.T. Sasaki, H. Tajiri, Y. Miura, T. Furubayashi, and K. Hono, Acta Mater. **142**, 49 (2018).

[10] T. Nakatani, S.K. Narayananellore, L.S.R. Kumara, H. Tajiri, Y. Sakuraba, and K. Hono, Scr. Mater. **189**, 63 (2020).